IEEE Access
Multidisciplinary ⋮ Rapid Review ⋮ Open Access Journal

Received 19 October 2023, accepted 20 November 2023, date of publication 24 November 2023,
date of current version 29 November 2023.

Digital Object Identifier 10.1109/ACCESS.2023.3336815

RESEARCH ARTICLE

A Compact Metamaterial Biosensor for Multi-Virus Detection With Tunability and High Incidence Angle Absorption

PATRI UPENDER[1], S. PRASANNA BHARATHI[1], SUKRITI[1], KRISHNA KUMBA[2], AND AMARJIT KUMAR[3], (Senior Member, IEEE)
[1]School of Electronics Engineering, Vellore Institute of Technology, Chennai, Tamil Nadu 600127, India
[2]School of Electrical Engineering, Vellore Institute of Technology, Chennai, Tamil Nadu 600127, India
[3]Department of Electronics and Communication, National Institute of Technology, Warangal, Telangana 506004, India

Corresponding author: Patri Upender (upender.p@vit.ac.in)

This work was supported by the Vellore Institute of Technology, Chennai, Tamil Nadu, India.

ABSTRACT In this research, we introduce a metamaterial biosensor designed for the detection of various viruses. The proposed sensor configuration comprises four square split ring resonators (SRR) coupled with a central graphene ring. The strong coupling between SRR and graphene ring results in near-perfect absorption at a frequency of 1.354 THz. To enhance versatility, the sensor's performance can be tuned and controlled by adjusting the chemical potential (μ_c) of the graphene. Additionally, we validate the sensor's functionality through an equivalent circuit model. Moreover, the proposed sensor demonstrates outstanding performance metrics, including a high sensitivity (S) of 1.7 THz/RIU, a Figure of Merit (FOM) of 165.09 RIU^{-1}, high-quality factor (Q) of 112.5. Despite its reduced structural thickness of 3 μm, it remains suitable for integration into nanotechnology devices. Furthermore, the absorber exhibits exceptional absorption properties even at steep incidence angles, expanding its applicability in diverse scenarios. Its potential to detect a wide range of viruses, including malaria, dengue, herpes simplex virus, influenza, and HIV, and distinguish various cancerous cells, holds promise for advancing biosensing applications.

INDEX TERMS Metamaterial, graphene, sensitivity, figure of merit, quality factor.

I. INTRODUCTION

In recent years, the field of terahertz (THz) sensing has experienced a resurgence of interest, driven by notable advancements in biosensor technology [1], [2]. Researchers have developed novel sensing techniques that leverage THz radiation to probe biological samples [3]. Various devices are employed within the THz frequency range, including antennas for transmitting and receiving EM waves, absorbers, sensors, spectrometry equipment, and imagery systems, each serving diverse applications [4], [5], [6], [7], [8], [9], [10]. THz waves can penetrate various non-metallic materials, including biological tissues, without causing harm [11], [12], [13]. This property makes THz radiation ideal for non-invasive and label-free sensing of biomolecules, cells, and tissues. Various types of absorbers are engineered to showcase distinct characteristics. Metamaterial absorbers are engineered to exhibit unique electromagnetic properties, including the ability to manipulate the absorption spectrum [9], [12], [14], [15]. This property enables them to selectively interact with specific THz frequencies associated with biomolecules, offering heightened sensitivity and selectivity in biosensing. While metals are often considered suitable materials for THz absorbers, their utility is limited due to issues related to weak conductivity and stability across spectral regions, particularly at longer wavelengths [16]. Additionally, metals are susceptible to degradation and rusting, rendering devices highly sensitive to temperature fluctuations and imposing constraints on their operational lifespan [17]. To address these challenges, some absorbers are designed

The associate editor coordinating the review of this manuscript and approving it for publication was Venkata Rajesh Pamula.

using metal-free materials, such as graphene, which not only offers tuning capabilities but also mitigates these shortcomings [7], [18], [19]. Furthermore, certain dielectric-based absorbers are tailored for biosensing applications, and characterized by relatively greater thickness compared to typical metamaterial absorbers [12], [20], [21], [22]. However, one drawback associated with dielectric-based absorbers is their tendency to necessitate a more substantial thickness and intricate structure, which can result in increased fabrication complexity. It is highly advisable to achieve a low or very low Full Width Half Maximum (FWHM) frequency response while maintaining a compact structure and simple design. Additionally, the pursuit of high S, a notably high FOM, and a substantial Q remains a formidable challenge. Moreover, the biosensors must possess the capability to detect a diverse range of diseases, including cancerous blood cells, malaria, and various chemicals. Various biosensors are employed for disease detection, encompassing ailments like TB, HIV, cancer, malaria, dengue and various biomedical applications [20], [23], [31], [24], [25], [26], [27], [15], [28], [29], [30]. In [23], an all-metal metamaterial absorber is introduced for biosensing applications, achieving a S of 0.5 THz/RIU, and an FOM of 23.5 RIU^{-1}. Furthermore, [24] emphasizes the potential of terahertz technology in detecting ultra-thin 7-nanometer dielectric films and presents a highly sensitive metamaterial sensor for ultrasensitive terahertz detection. Additionally, in [25], a highly sensitive plasmonic sensing device is developed, employing a fishnet structure based on a circular hole array, with promising applications in enhancing refractive index detection for bio-applications. In [27], the authors proposed a metamaterial absorber comprising an array of split ring resonators for THz applications yielding an S of 0.3 THz/RIU, and FOM of 2.94 RIU^{-1}. In [15], the authors have demonstrated sensing capabilities utilizing toroidal resonance in a two-dimensional terahertz metamaterial, where mirrored asymmetric Fano resonators possess anti-aligned magnetic moments at an electromagnetic resonance, resulting in a toroidal dipole. Furthermore, the researchers in [28] introduce two distinct perfect metamaterial absorbers as sensors in the THz regime, achieving a maximum FOM of 2.3 RIU^{-1} and S of 0.007 THz/RIU for an analyte thickness of 16 μm. Moreover, [29], investigates a metamaterial absorber capable of detecting cancerous cells for biomedical applications, demonstrating a S of 1.47 THz/RIU, FOM of 36.17 RIU^{-1}, and Q of 92.75. Many of these sensors are either electrochemical or optical in nature. Despite their accuracy and precision, these sensors come with notable limitations. Some of these sensors exhibit subpar performance concerning key metrics such as S, FOM, and Q, which are crucial for biosensing applications. Additionally, these sensors possess intricate structures that pose challenges in the fabrication process, while few sensors require sample purification, others rely heavily on laboratory research, and a few are characterized by bulkier dimensions.

In outline, the uniqueness of this investigation stems from the configuration of our proposed sensor, which encompasses several noteworthy aspects: (i) The development of a Metamaterial-based biosensor with the capability to detect a wide range of viruses, including dengue, malaria, HIV, cancer, HSV, and Influenza A. (ii) Significantly decreasing the thickness of the absorber to guarantee alignment with nanotechnology sensors. (iii) Achieving good performance parameters, including ultra-precise and narrow absorption characteristics, tailored specifically for biosensing applications. (iv) Crafting a simple design to alleviate manufacturing complexities. (v) The introduction of tunability in the sensor's response. (vi) Demonstrating high absorption even at steep incidence angles. These facets collectively contribute to the uniqueness and innovation of our research in the field of biosensors.

II. PROPOSED ABSORBER DESIGN

A novel absorber structure is proposed, and its unit cell is illustrated in Fig. 1(a). At the base of the absorber structure, a Graphene (Gr) sheet is positioned. This graphene sheet serves as a perfect reflector, effectively bouncing incident electromagnetic waves back towards the absorber. The periodicity of this Gr sheet is defined as $W_g \times L_g (80 \times 80) \mu m$. Positioned on top of the Gr sheet is a substrate composed of silicon dioxide (SiO_2). The substrate material has a permittivity (ε_s) value of 2.25. It plays a crucial role in manipulating the electromagnetic waves. The substrate has a defined thickness (t_s) and dimensions in width and length, denoted as $W_s \times L_s (80 \times 80) \mu m$. On top of the SiO_2 layer, four square split rings made of gold (Au) (SGSR) having a conductivity of $\sigma = 5.8 \times 10^7 S/m$ are strategically placed. These split rings are designed with inner and outer radii $r_{is}$and r_{os}, respectively and have a split gap (g_s) measuring 4 μm. The gold-based split rings are key elements for absorbing and dissipating electromagnetic energy within the desired frequency range. At the center and top of the substrate, a circular ring made of graphene is positioned. This circular graphene ring (CGR) has inner and outer radii of g_{ir} and g_{or}, respectively. It plays a vital role in enhancing the absorber's performance by further manipulating the incident electromagnetic waves. Fig. 1(b) shows the periodic pattern of the proposed structure. The side view of the proposed structure with and without graphene is depicted in Fig. 1(c), and 1(d). The ion-gel layer (IGL), with a permittivity of 1.852, placed over the meta structure, facilitates simultaneous biasing of all periodically structured unit cells, enhancing their collective performance in absorbing incident electromagnetic waves and achieving adjustability and controllability in the absorber characteristics. The equivalent circuit (EC) representation of the proposed absorber is depicted in Fig. 1(e) [20], [32], [33]. The EC is divided into four parts: (i) Substrate (SiO_2), (ii) Ion-gel, (iii) SGSR, and (iv) CGR. The initial component corresponds to a shorted wired line featuring a SiO_2 with a thickness denoted as t_s strategically positioned on the ground plane. This element yields the input impedance, as delineated in equation (1).

$$Z_a = jZ_{si} tan\gamma_s t_s \tag{1}$$

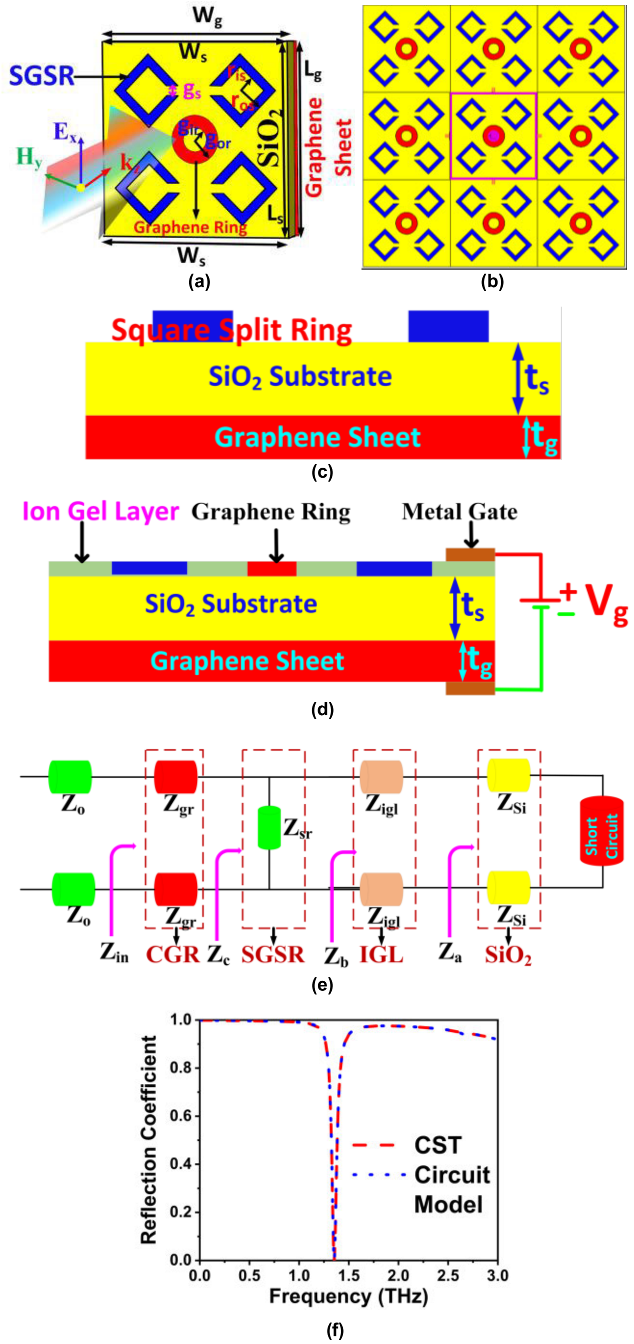

FIGURE 1. **Proposed absorber (a) with incident THz wave, (b) Periodic pattern, (c) Without graphene, (d) With Graphene ring and biasing, (e) equivalent circuit mode, and (f) CST Vcc EC.**

where $\gamma_s = (\omega/c)\,(\varepsilon_s)^{1/2}$ is the propagation constant and $Z_{si} = Z_o\big/\,(\varepsilon_s)^{1/2}$is the impedance of the silicon dioxide substrate, and Z_o is the free space impedance. In the second part, the IGL layer is evaluated using equation (2).

$$Z_b = Z_{igl}\frac{[Z_a + jZ_{igl}tan\gamma_i h_g]}{[Z_{igl} + jZ_a tan\gamma_i h_g]} \tag{2}$$

In the above equation, $\gamma_i = (\omega/c)\,\left(\varepsilon_{igl}\right)^{1/2}$is the propagation constant, and $Z_{igl} = Z_o\Big/\left(\varepsilon_{igl}\right)^{1/2}$ is the impedance shown by the IGL. Next, SGSR exhibits a Z_s impedance and can be modelled using an RLC circuit. The total input impedance of the EC is $Z_{in} = Z_{gr} + Z_c$.

Here $\boldsymbol{Z_{gr}} = (\boldsymbol{R_{CGR}} + \boldsymbol{j\omega L_{CGR}}) \approx \boldsymbol{1\big/\alpha_{CGR}}$is the impedance of CGR, and $\boldsymbol{Z_c} = \boldsymbol{Z_{sr}} \parallel \boldsymbol{Z_b}$. The reflection coefficient is determined using $\boldsymbol{\Gamma} = (\boldsymbol{Z_{in}} - \boldsymbol{Z_0})\big/(\boldsymbol{Z_{in}} + \boldsymbol{Z_0})$. Finally, the computed reflection coefficient is plotted and depicted in Fig. 1(f). The results obtained from both CST and ECD simulations are presented, highlighting a notable level of concurrence between the two simulation tools. This agreement serves as strong validation for the operational integrity of the analyzed configuration. The absorption and reflection plots of the proposed absorber with and without CGR are depicted in Fig. 2 (a), and Fig. 2(b). The Absorption coefficient (A) is determined using the equation A = 1 - R - T, where R signifies the Reflection coefficient, and T denotes the Transmittance.

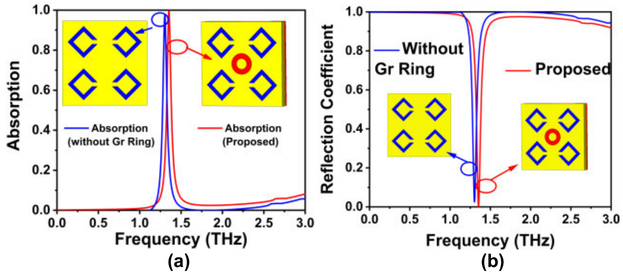

FIGURE 2. **Proposed absorber with and without Gr ring (a) Absorption plot, (b) reflection plot.**

Here, the graphene sheet at the bottom of the design effectively eliminates Transmittance (T≈0). Consequently, for absorption to approach unity (A≈1), the Reflectance (R) must be minimized to the greatest extent possible.

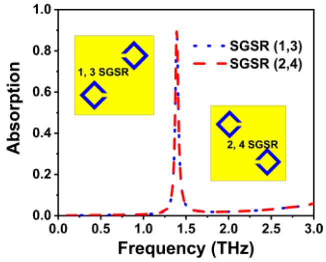

FIGURE 3. **Absorption plot for SGSR (1,3), and SGSR (2,4).**

The absorber without CGR exhibits an absorption of 99.887% at a frequency of 1.302 THz. With the addition of CGR, the absorber shifts the resonant frequency (f_{res}) and exhibits an enhanced absorption of 99.998% at a frequency of 1.354 THz. The addition of CGR not only enhances the absorptivity but also tunes the f_{res}. The addition of graphene enhances absorption because graphene is a highly conductive material that can efficiently convert incident electromagnetic energy into heat due to its unique electrical properties. Furthermore, Graphene's conductivity leads to a stronger interaction with incident electromagnetic waves, allowing for improved absorption of energy from these waves. The incorporation of CGR introduces tunability and enhances the absorber's frequency response by enabling adjustments in external electrostatic bias while considering the electrical properties of CGR sourced from the literature [34], [35], where an initial chemical potential (μ_c) of $\mu_c = 0$ eV at $T = 300$ K and a relaxation time (τ) of $\tau = 0.1$ ps is applied. The Computer Simulation Technology (CST) Microwave Studio is employed for the simulation and optimization of the proposed absorber's dimensions. Cell boundary conditions are established in the x and y directions, while open boundary conditions are defined in the z direction. The absorption plot in Fig. 3 illustrates the absorber's performance while considering two sets of rings: SGSR (1, 3) and SGSR (2, 4), with each set consisting of two rings. In this configuration, the plot reveals an absorptivity of 90%. This behavior can be attributed to the fact that when the absorber structure incorporates only two rings at a time, the incident electromagnetic (EM) waves do not induce a high electromagnetic distribution as compared to the absorber equipped with four SGSR's. In essence, the reduced number of rings results in a lesser capacity to capture and dissipate the incident EM energy, leading to a lower absorptivity of 90%.

III. VARIATION IN PHYSICAL PARAMETERS

In this section, we delve into the behavior of the proposed absorber when subjected to variations in physical parameter dimensions. This investigation allows us to gauge the effectiveness of the absorber's performance. Notably, we focus on altering a single parameter while keeping all other parameters constant.

A. SUBSTRATE THICKNESS (T_S)

Initially, we validate the absorber's performance concerning variations in substrate thickness (t_s). During this investigation, we systematically vary t_s, ranging from 2 μm to 4 μm in increments of 0.5 μm as shown in Fig. 4(a). What we observe is that when t_s is at lower values, the absorber tends to exhibit lower absorptivity, whereas when t_s is increased to higher values, it results in a broader bandwidth of absorption. Particularly noteworthy is the fact that when t_s is set at 3 μm, the absorber attains a state of perfect absorption, characterized by a notably narrow absorption spectrum.

B. SPLIT GAP (G_S)

The next parameter under investigation is the SGSR split gap (g_s), which we vary within a range from 0 to 4 μm, incrementing it by 1 μm at each step as depicted in fig. 4(b). Here t_s is set to 3 μm, set from the above investigation. What we observe is that as g_s increases, the f_{res} tends to shift toward the higher frequency range and fails to achieve perfect absorption. Notably, when g_s is set at 2 μm, the absorber achieves a near-perfect absorption rate of 99.998%.

C. SPLIT OUTER RADIUS OF SGSR (R_{SO})

The next parameter under investigation is the outer radius of SGSR (r_{so}), which is varied within the range of 38 μm to 42 μm, with each step incrementing by 1 μm, as depicted in Fig. 4(c). What we observe is that when r_{so} is set at 40 μm, the absorber achieves a state of near-perfect absorption characterized by a notably narrow bandwidth. However, for both higher and lower values of r_{so}, the absorber exhibits low absorption with high bandwidth.

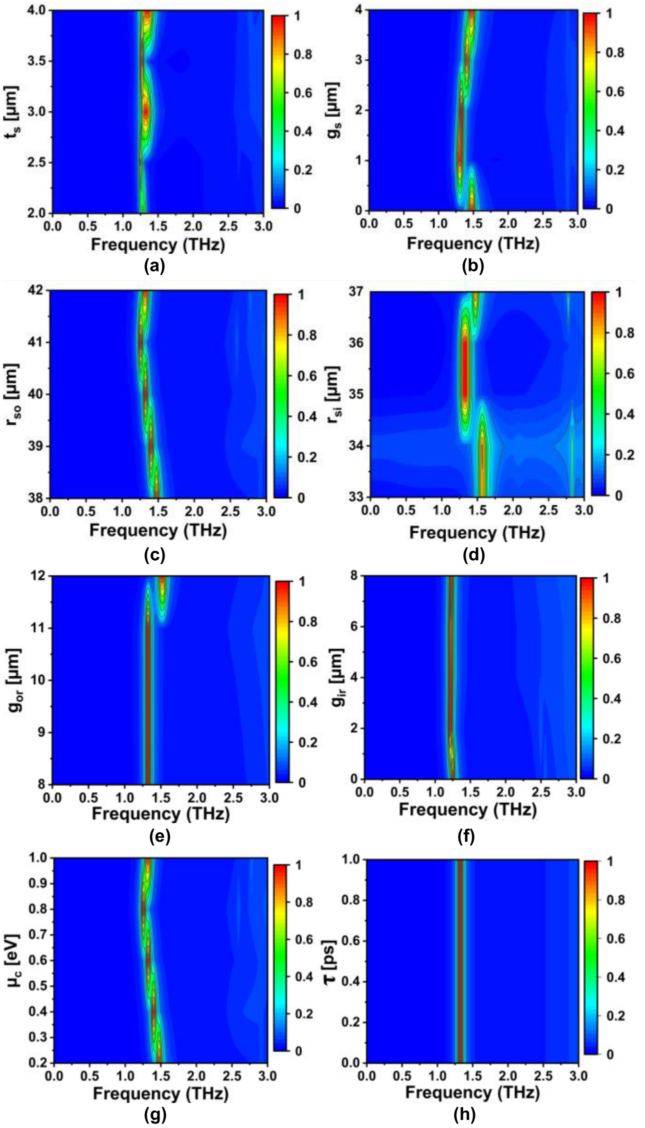

FIGURE 4. Absorption plot for changes in parameters, (a) t_s, (b) g_s, (c) r_{so}, (d) r_{si}, (e) g_{or}, (f) g_{ir}, (g) μ_c, and (h) T.

D. INNER RADIUS OF SGSR (R_{SI})

In the subsequent investigation, we vary the inner radius of the SGSR (r_{si}) within the range of 33 μm to 37 μm, incrementing it by 1 μm at each step. Our findings indicate that when r_{si} is set at 35 μm, the absorber reaches a state of near-perfect absorption, characterized by a narrow bandwidth, as depicted in Fig. 4(d). However, for other values of r_{si}, we observe a slight decrease in the level of absorption.

E. OUTER RADIUS OF CGR (G_{OR})

Next, we explore the impact of varying the outer radius of CGR (g_{or}) within the range of 8 to 12 μm, with each step incrementing by 1 μm. Our observations indicate that as g_{or} increases to higher values, the absorber exhibits reduced absorption. However, at g_{or} equal to 10 μm, we observe a remarkable absorption rate of 99.998%, accompanied by a narrow spectral bandwidth.

F. INNER RADIUS OF CGR (G_{IR})

Next, the inner radius of CGR (g_{ir}) is varied from 0 to 8 μm at a period variation of 1 μm. It is noticed that for $g_{ir} = 4$ μm, the absorber exhibits near-perfect absorption with a narrow spectral bandwidth.

G. CHEMICAL POTENTIAL OF CGR (μ_c)

Next, the impact of changing the chemical potential of graphene (μ_c) on the absorber's performance within a range spanning from 0.2 eV to 1 eV is investigated, with each step incrementing by 0.1 eV, as depicted in Fig. 4(g). Our observations reveal that as μ_c increases, there is a noticeable shift in the f_{res} toward lower frequencies. Changing μ_c of CGR influences its carrier concentration and, consequently, its electrical properties, including its ability to support surface plasmon resonances, thereby influencing its interaction with incident electromagnetic waves and enabling precise control of the absorption spectra to match the operational needs.

H. RELAXATION TIME OF CGR (τ)

In the subsequent analysis, we explore the influence of varying the graphene relaxation time (τ) across a range from 0 ps to 1 ps in increments of 0.2. What we observe is that, regardless of the changes in τ, the absorption characteristics of the absorber remain consistent. The introduction of graphene enhances absorption without altering the number of resonant peaks. Consequently, for all values of τ, the absorber's performance remains unaffected, maintaining a constant f_{res} and absorption rate throughout the parameter variations.

IV. FIELD DISTRIBUTION

In Fig. 5, the electric field (E) distribution is depicted across the proposed absorber in different planes, at Z=0, Z=d, and Y=0 at the f_{res} of 1.354 THz. This visual representation of the electric field distribution, obtained through comprehensive full-wave simulation, serves as compelling evidence, highlighting the prominent concentration of a high magnitude of the electric field within the metallic resonators and the graphene ring. This observation underscores the absorber's exceptional efficacy in capturing and precisely manipulating electromagnetic energy within these specified regions. The magnetic field (H) distribution, as illustrated in Fig. 6, provides us with a comprehensive insight into the absorber's EM behavior in different spatial planes, at the Z=0, Z=d, and Y=0 positions at f_{res} of 1.354 THz. This distribution elucidates the presence of a substantial H intensity across all these planes, affirming the absorber's exceptional ability to capture, manipulate, and effectively absorb incident electromagnetic waves. The high H concentration observed in these planes is a direct consequence of the absorber's structural configuration and material properties. The metallic resonators and CGR within the absorber structure exhibit strong magnetic responses due to their respective geometric shapes and electrical conductivity. The interaction of incident EM waves with these components induces localized currents and magnetic fields, which, in turn, contribute to the observed high magnetic field intensity.

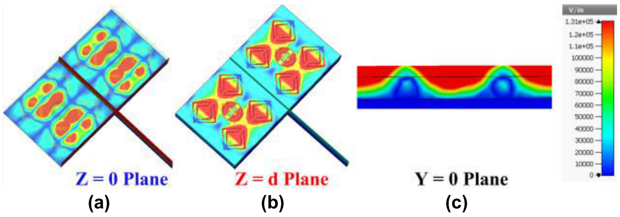

FIGURE 5. ED at different planes of (a) Z = 0, (b) Z= d, (c) Y = 0.

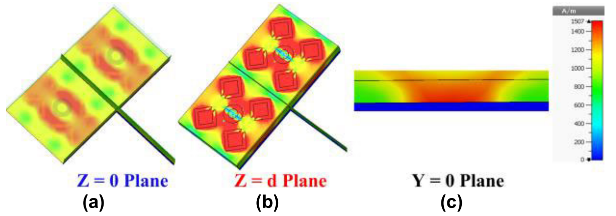

FIGURE 6. H distribution at different planes of (a) Z = 0, (b) Z= d, (c) Y = 0.

Fig. 7 provides a detailed depiction of the surface current distribution, offering insights into the behavior of EM waves on both the graphene sheet plane (Z=0) and the SGSR plane (Z=d). This distribution reveals an intriguing phenomenon: the presence of significant charge accumulation on both the SGSR and the CGR. This observation carries profound implications for the absorber's strong EM absorption capabilities.

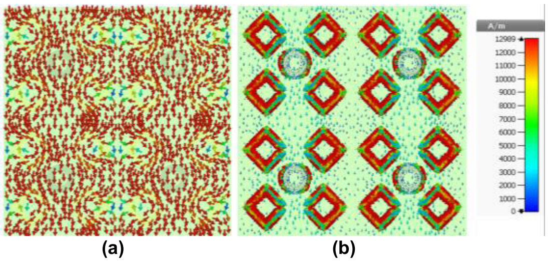

FIGURE 7. Surface distribution at different planes of (a) Z = 0, (b) Z= d.

The strong charge accumulation on the SGSR is indicative of their role as efficient resonators. These metallic rings are adept at capturing incident electromagnetic waves and subsequently channeling them into localized current loops. This resonance phenomenon not only enhances the absorber's absorption efficiency but also demonstrates its ability to concentrate EM energy within the SGSR regions. Simultaneously, the charge accumulation on the CGR further accentuates the absorber's exceptional performance. Graphene, renowned for its high electrical conductivity, actively participates in this charge accumulation process.

V. STABILITY ANALYSIS

The performance of the proposed sensor undergoes stability analysis, which is crucial for assessing its reliability and consistent behavior. In Fig 8(a), the absorption characteristics for both TE (Transverse Electric) and TM (Transverse Magnetic) polarizations are exhibited. Notably, owing to the inherent symmetry of the absorber structure, it exhibits identical absorption characteristics with remarkably narrow absorption bandwidths for both TE and TM incident waves. Fig. 8(b), depicts absorption spectra for different incident angles (θ). A notable shift in f_{res} towards lower values as θ varies, with the absorber consistently achieving absorption rates exceeding 85% up to $\theta = 70^o$, followed by a modest reduction to approximately 80% for higher incident angles. This adaptability to a range of angles while maintaining high absorption efficiency is advantageous in real-world applications where incident EM waves may arrive at varying θ, further emphasizing the versatility and effectiveness of the proposed absorber in EM wave management.

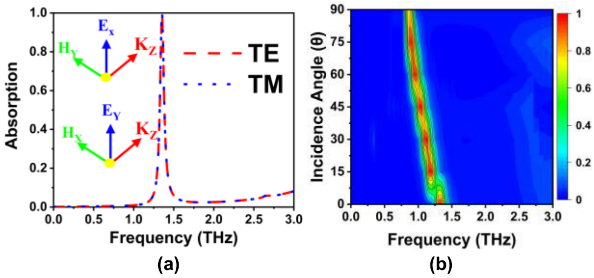

FIGURE 8. **Frequency response for (a) TE and TM polarization, and (b) Various incident angles.**

VI. SENSING PERFORMANCE

A. RI SENSING

The proposed absorber demonstrates exceptionally narrow absorption spectra, characterized by a FWHM of 0.011 THz, resulting in an impressively high-quality factor (Q) of 112.5, attributes that render it exceptionally suitable for applications in THz virus detection, including but not limited to malaria, dengue, and influenza viruses. In Fig. 9(a), the illustration depicts the presence of the analyte (test medium) positioned atop the proposed absorber. Initially, specific analyte thickness (ta) and refractive indices (RI) are chosen for detecting various viruses. As demonstrated in Fig. 9(b), the frequency response exhibits excellent performance across a range of RI values, spanning from 1 to 2 in increments of 0.2, while maintaining a constant ta of 1 µm. The corresponding plots in Fig. 9(c) depict the variation in Δf (Shift in f_{res}) and sensitivity (S), calculated using the formula $S = \Delta f / \Delta n [THz/TU]$, where Δn represents the change in RI. Notably, a maximum sensitivity (S) of 1.595 THz/TU is achieved at an RI of n=1.6. Fig. 9(d) further showcases the plots of FWHM and FOM, with FOM calculated using the equation $FOM = S / FWHM (RIU^{-1})$. Impressively, a peak FOM of 160 RIU^{-1} is attained at an RI value of n=1.6. These findings collectively affirm the proposed absorber's exceptional suitability for high-performance RI-based virus detection applications in the THz spectrum.

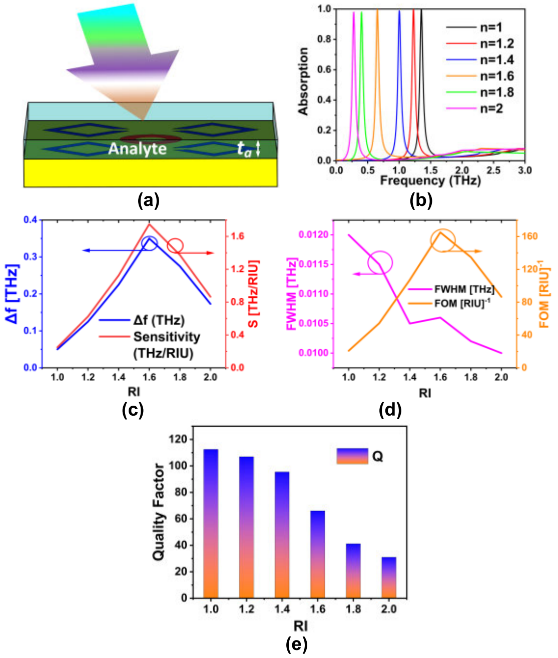

FIGURE 9. **Sensing performance (a) Analyte on top, (b) RI sensing, (c) Δf, S, (d) FWHM, FOM, (e) Q.**

The sensor performs well for different values of RI as shown in the plots (Fig. 9(c)) of Δf (Shift in f_{res}), and sensitivity (S). S is determined using the expression, $S = \Delta f / \Delta n [THz/TU]$, where Δn is the change in RI. A maximum S of 1.595 THz/TU is observed for n=1.6. Fig. 9(d) illustrates the plots of FWHM and FOM. FOM is calculated using the equation, $FOM = S / FWHM (RIU^{-1})$. A maximum FOM of 160 RIU^{-1} is observed for n=1.6. The plot of Q is depicted in Fig. 9(e). Q is determined by employing the formula, $Q = f_{res} / FWHM$. The results of S, FOM, and Q collectively establish the proposed sensor as an exceptionally promising candidate for biosensing applications, offering high S, impressive FOM, and a superior Quality factor, thereby demonstrating its potential for precise and efficient virus detection and related biomedical applications in the THz frequency range.

B. T_A SENSING

The performance of the proposed sensor showcases its versatility and effectiveness across a range of analyte thicknesses

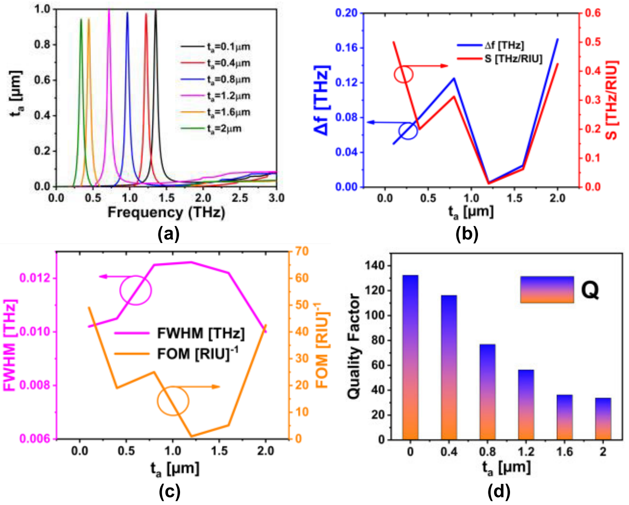

FIGURE 10. Sensing parameters (a) Analyte on top, (b) RI sensing, (c) Δf, S, (d) FWHM, FOM, (e) Q.

(t_a), spanning from 0.1 μm to 2 μm, as visually presented in Fig. 10(a).

Throughout this range, the sensor consistently demonstrates strong performance, reflected in its commendable values for S, Full-Width Half Maximum (FWHM), FOM, and Q, as depicted in Fig. 10. Whether dealing with thinner or thicker analyte layers, the sensor maintains its strong attributes, making it a robust choice for biosensing and detection applications where varying analyte conditions may be encountered.

C. VIRUS SENSING

The absorber has been investigated for its capacity to detect a diverse range of viruses, encompassing malaria, dengue, HSV (Herpes Simplex Virus), Influenza A, HIV (Human Immunodeficiency Virus), coronavirus, various cancer cells, as detailed in Table 1. In the case of malaria detection, where infected Red Blood Cell (RBC) specimens exhibit varying refractive indices (n_1 and n_2) at different stages of infection, with values of $n_1 = 1.373$ and $n_2 = 1.383$, the importance of early detection is paramount due to the potentially life-threatening consequences [36], [37]. The proposed sensor exhibits exceptional performance in the detection of malaria-infected RBCs, manifesting a remarkable S of 0.536 and 0.561 THz/RIU, a high FOM of 49.64 TU^1, and a high Q of 101.851.

For sensing the Dengue virus, a highly dangerous pathogen with an n of 1.4, the proposed sensor showcases impressive performance in its detection [38], [39]. It delivers notable values for S, FOM, and Q, underlining its efficacy in swiftly and accurately detecting the presence of the Dengue virus. This outstanding performance underscores the sensor's potential as a critical tool for the early detection of malaria, a disease that can have life-threatening consequences [40].

TABLE 1. Virus detection.

Virus	RI	Δf	Δn	S	FWHM	FOM	Q
malaria (n_1)	1.373	0.2	0.373	0.5361	0.0108	49.6475	101.85
malaria (n_2)	1.383	0.215	0.383	0.5613	0.0105	53.4626	100
Dengue	1.4	0.225	0.4	0.5625	0.0102	55.1470	98.039
HSV	1.41	0.23	0.41	0.5609	0.0106	52.9222	96.226
Influeza A	1.48	0.3	0.48	0.625	0.0104	60.0961	86.538
HIV	1.5	0.32	0.5	0.64	0.0102	62.7451	86.274
Corona	1.53	0.34	0.53	0.6415	0.0101	63.5157	84.158
Virus	RI	Δf	Δn	S	FWHM	FOM	Q
Human blood (healthy)	1.35	0.185	0.35	0.528	0.0102	51.82	108.8235
Basal cell (cancerous)	1.38	0.229	0.42	0.59	0.0101	55.147	98.03922
Basal cell (normal)	1.36	0.197	0.38	0.5184	0.0103	50.332	105.8252
Normal breast cell (MDAM D-231)	1.385	0.22	0.385	0.571	0.0105	54.4217	103.5714
Cancer breast cell (MDAM D-231)	1.399	0.225	0.399	0.5639	0.0099	56.960	112.12
Normal cervical cell	1.368	0.191	0.368	0.5190	0.0104	49.905	105.6731
Cervical Cancer cell	1.392	0.222	0.392	0.5663	0.0096	58.992	115.31
Jurkat (cancerous)	1.39	0.223	0.39	0.5717	0.0102	56.058	107.8431
Jurkat (normal)	1.376	0.205	0.376	0.5453	0.0103	52.933	105.5146
Normal breast cell (MCF-7)	1.3663	0.189	0.36	0.525	0.0104	50.480	104.3846
PC12 cell	1.381	0.198	0.381	0.519	0.0101	51.453	107.6733
HSC	1.844	0.4	0.844	0.4739	0.01	47.393	83
CSC	2.049	0.5	1.049	0.4766	0.011	43.331	74.54

Herpes Simplex Virus (HSV) is a common and contagious virus that can affect humans. There are two main types of HSV: HSV-1, which primarily causes oral herpes (cold sores), and HSV-2, which typically causes genital herpes [40]. Alarming statistics reveal that HSV-1 infects up to 90% and HSV-2 affects approximately 25% of the global population, imposing a significant burden of morbidity and mortality.

TABLE 2. Comparison with other research articles.

Ref	Bands	f (THz)	S (THz/TU)	FOM (RIU^{-1})	Q	Thickness (µm)	Polarization Insensitivity	Tunability	Design Method
[23]	1	2	0.5	23.5	87	33	No	No	Metamaterial
[24]	1	1	0.016	-	-	25	No	No	Metamaterial
[25]	1	0.557	-	1.5	7	50	No	No	Metamaterial
[27]	1	2.249	0.3	2.94	22.04	10.4	No	No	Metamaterial
[15]	1	0.4	0.0273	-	9.6	502	No	No	Metamaterial
[28]	1	0.6	0.007	2.3	11.6	518.2	Yes	Yes	Metamaterial
[29]	1	3.71	1.47	36.17	92.75	8.4	Yes	No	Metamaterial
Proposed	**1**	**1.354**	**1.7**	**165.09**	**112.5**	**3**	**Yes**	**Yes**	**Metamaterial**

The transmission of the virus primarily occurs through direct contact with the host's mucous membranes. While clinical presentations offer valuable clues for HSV identification, diagnostic accuracy may diminish as the disease progresses, necessitating laboratory confirmation for precision. In this context, we introduce the proposed sensor designed for the early detection of HSV, as detailed in Table 1. Notably, this sensor exhibits robust performance, establishing its potential utility as a reliable tool for the accurate detection of this virus, thereby addressing a critical need in the field of medical diagnostics.

Type "A" influenza viruses are the probable prime origin of the ailment referred to as avian influenza (A), commonly recognized as bird flu. Wild aquatic birds are the probable origin and conveyors of numerous viruses, and ailments in these creatures typically do not display symptoms. This virus is commonly transferred when an individual is near an infected or dead bird. Early viral diagnosis can potentially affect the patient's treatment [30]. Here, we employ the suggested sensor to detect this virus. Table 1 indicates that the proposed sensor can effectively detect the virus, displaying a good S, a good FOM, and a substantial Q.

The refractive index (n) of coronaviruses (CV) is closely associated with that of other viruses, particularly murine leukemia viruses, owing to their shared core/shell structural characteristics. Notably, this n is intricately linked to virus size. Given the variability in size observed in coronaviruses, which can range from smaller to larger configurations, the refractive index can span an approximate range of 1.47 to 1.53 [41]. For our analysis, we approximate the n of CV as 1.53. Under this assumption, the proposed sensor yields outstanding results, demonstrating a remarkably high S of 0.641 THz/RIU, an impressive FOM of 63.51 TU^{-1}, and a substantial Q of 84.15. These results position the sensor as an effective tool for the precise detection of CV, underscoring its potential value in applications related to virus identification and monitoring. However, it is essential to recognize that clinical laboratory experiments remain indispensable for the definitive confirmation of the CV virus.

The proposed sensor delivers exceptional performance in detecting the various cancerous viruses such as, Human blood (healthy) having RI of 1.35, Basal cell (cancerous) having RI of 1.38, Basal cell (normal) having RI of 1.36, Normal breast cell (MDAMD-231) having RI of 1.385, Cancer breast cell (MDAMD-231) having RI of 1.399, Normal cervical cell having RI of 1.368, Cervical cancer cell having RI of 1.392, Jurkat (cancerous) having RI of 1.39, Jurkat (normal) having RI of 1.376, Normal breast cell (MCF-7) having RI of 1.363, PC12 cell having RI of 1.381, Healthy Skin cells (HSC) having RI of 1.844, Cancerous Skin Cells (CSC) having RI of 2.049 [42], [43], [44]. The sensor's exceptional performance across this diverse range of cancerous viruses and cells, each characterized by its unique RI, underscores its potential as a versatile diagnostic tool for detecting and distinguishing various pathological conditions as depicted in Table 2.

This capability has significant implications for disease diagnosis, treatment monitoring, and biomedical research, ultimately contributing to advancements in healthcare and medical science. The performance of the proposed sensor has been systematically evaluated and compared to that of other similar research articles, as detailed in Table 2. Notably, the results demonstrate that the proposed sensor outperforms these previous investigations in terms of S, FOM, and Q. Thus, the proposed sensor demonstrates outstanding performance, showcasing its potential to advance sensor technology across a range of applications, especially in virus and cell detection. The enhanced sensitivity, precision, and overall effectiveness, as indicated by improved S, FOM, and Q values, position it as a valuable addition to the field of biomedical and diagnostic sensing. Finally, it is necessary to report the fabrication steps for the proposed sensor as there is a significant scope in the present and near future. Initially, a clean SiO_2 substrate is selected as the foundation for the biosensor. Subsequently, a graphene layer is grown on one side of the SiO_2 substrate using the thermal evaporation method or by using the chemical vapor deposition method. On the top of the SiO_2 layer, a graphene layer can be etched via the thermal evaporation technique. The unwanted graphene can be etched away using reactive ion etching (RIE) to create a circular graphene ring. Following this, a thin layer of gold (Au) is uniformly deposited across the entire substrate. This deposition is further refined by employing a second lithography step, during which the lithography masks serve the pivotal role of safeguarding the central graphene ring while revealing the regions where the split rings are intended to be situated. Continuing the process, the exposed gold is diligently etched away through an appropriate etching process, meticulously preserving only the four-square split rings and the central circular graphene ring. This intricate procedure aligns with photolithography techniques grounded in large-scale microfabrication principles. Next, an ion-gel layer is deposited above the structure of the graphene ring placed on the substrate. This can be accomplished using the thermal evaporation method. Concurrently, a metal gate is grown on the edge of the absorber unit cell. This metal gate is essential for connecting the bias voltage to the biosensor. A thorough inspection is conducted on the fabricated metamaterial biosensor to check for defects, ensure proper dimensions, and assess the quality of the patterns. An initial phase of electrical testing is employed to verify the functionality of the biosensor. The biosensor is subsequently integrated into the broader THz sensing system, where it undergoes exhaustive testing, accommodating THz sources and a plethora of sample variations. This comprehensive testing protocol serves to provide an exhaustive characterization of the sensor's performance across multiple scenarios and applications. Finally, the sensor is fine-tuned and its parameters and design are optimized as necessary to achieve the desired sensitivity and selectivity for virus detection and biosensing applications.

VII. CONCLUSION

In conclusion, this research presents a metamaterial biosensor with good performance capabilities for the detection of a wide range of viruses. The sensor's innovative design, consisting of four SGSR coupled with a CGR, offers near-perfect absorption at a frequency of 1.354 THz. What sets this sensor apart is its adaptability, as it can be finely tuned by adjusting the μ_c of the graphene, providing versatility for various applications. Through rigorous validation using an EC model, we have established the sensor's reliability and functionality. The outstanding performance metrics speak volumes about its potential impact in the field of biosensing. The sensor exhibits a high S of 1.7 THz/RIU, an impressive FOM of 165.09 RIU^{-1}, and a substantial high Q of 112.5. Moreover, its compact structural thickness of just 3 μm makes it suitable for integration into nanotechnology devices, opening exciting possibilities for miniaturized and highly efficient biosensing systems. Furthermore, the sensor's exceptional absorption properties even at steep incidence angles broaden its applicability, making it an asset in diverse scenarios. Its potential to detect a wide range of viruses, including malaria, dengue, herpes simplex virus, influenza, HIV, and coronaviruses, as well as its ability to distinguish various cancerous cells, holds promise for advancements in biosensing applications.

REFERENCES

[1] H.-J. Song and N. Lee, "Terahertz communications: Challenges in the next decade," *IEEE Trans. Terahertz Sci. Technol.*, vol. 12, no. 2, pp. 105–117, Mar. 2022, doi: 10.1109/TTHZ.2021.3128677.

[2] K. Li and J. Yu, "Photonics-aided terahertz-wave wireless communication," *J. Lightw. Technol.*, vol. 40, no. 13, pp. 4186–4195, Jul. 2022, doi: 10.1109/JLT.2022.3161878.

[3] M. Gezimati and G. Singh, "Terahertz imaging and sensing for healthcare: Current status and future perspectives," *IEEE Access*, vol. 11, pp. 18590–18619, 2023, doi: 10.1109/ACCESS.2023.3247196.

[4] P. Upender and A. Kumar, "Quad-band circularly polarized tunable graphene based dielectric resonator antenna for terahertz applications," *Silicon*, vol. 14, no. 10, pp. 5513–5526, Aug. 2021, doi: 10.1007/s12633-021-01336-5.

[5] P. Upender and A. Kumar, "Circularly polarized 2×2 MIMO dielectric resonator antenna for terahertz applications," in *Proc. IEEE Indian Conf. Antennas Propag. (InCAP)*, Dec. 2021, pp. 283–286, doi: 10.1109/InCAP52216.2021.9726292.

[6] P. Upender and A. Kumar, "$\text{HEM}_{11\delta}$ and $\text{HEM}_{12\delta}$-based quad band quad sense circularly polarized tunable graphene-based MIMO dielectric resonator antenna," *Frequenz*, vol. 76, nos. 5–6, pp. 273–285, Jun. 2022, doi: 10.1515/freq-2021-0145.

[7] P. Upender and A. Kumar, "Graphene-based ultra-wideband absorber for terahertz applications using hexagonal split ring resonators," *Phys. Scripta*, vol. 97, no. 6, Jun. 2022, Art. no. 065503, doi: 10.1088/1402-4896/ac6af1.

[8] R. Singh, W. Cao, I. Al-Naib, L. Cong, W. Withayachumnankul, and W. Zhang, "Ultrasensitive terahertz sensing with high-Q Fano resonances in metasurfaces," *Appl. Phys. Lett.*, vol. 105, no. 17, Oct. 2014, Art. no. 171101, doi: 10.1063/1.4895595.

[9] J. Wu, T. Yuan, J. Liu, J. Qin, Z. Hong, J. Li, and Y. Du, "Terahertz metamaterial sensor with ultra-high sensitivity and tunability based on photosensitive semiconductor GaAs," *IEEE Sensors J.*, vol. 22, no. 16, pp. 15961–15966, Aug. 2022, doi: 10.1109/JSEN.2022.3190414.

[10] M. A. Assou, G. Humbert, A. Crunteanu, and C. Decroze, "Synthetic photoconductive antenna array for terahertz 3-D imaging and spectroscopy," *IEEE Trans. Terahertz Sci. Technol.*, vol. 13, no. 5, pp. 440–447, Sep. 2023, doi: 10.1109/TTHZ.2023.3281771.

[11] P. Upender and A. Kumar, "A new technique for Hexa band quad sense cylindrical dielectric resonator antenna for THz applications," in *Proc. IEEE IAS Global Conf. Emerg. Technol. (GlobConET)*, May 2023, pp. 1–5, doi: 10.1109/GlobConET56651.2023.10149946.

[12] P. Upender and A. Kumar, "Highly sensitive tunable dual-band THz refractive-based metamaterial sensor for biosensing applications," *IEEE Trans. Plasma Sci.*, vol. 51, no. 10, pp. 3258–3264, Oct. 2023, doi: 10.1109/TPS.2023.3314536.

[13] P. Upender and A. Kumar, "Implementing reconfigurable circularly polarized two port MIMO DRA for THz applications," *Opt. Quantum Electron.*, vol. 55, no. 10, pp. 1–23, Oct. 2023, doi: 10.1007/s11082-023-05188-8.

[14] W. Pan, T. Shen, Y. Ma, Z. Zhang, H. Yang, X. Wang, X. Zhang, Y. Li, and L. Yang, "Dual-band and polarization-independent metamaterial terahertz narrowband absorber," *Appl. Opt.*, vol. 60, no. 8, pp. 2235–2241, Mar. 2021, doi: 10.1364/ao.415461.

[15] M. Gupta, Y. K. Srivastava, M. Manjappa, and R. Singh, "Sensing with toroidal metamaterial," *Appl. Phys. Lett.*, vol. 110, no. 12, Mar. 2017, Art. no. 121108, doi: 10.1063/1.4978672.

[16] R. Xu, X. Liu, and Y.-S. Lin, "Tunable ultra-narrowband terahertz perfect absorber by using metal-insulator-metal microstructures," *Results Phys.*, vol. 13, Jun. 2019, Art. no. 102176, doi: 10.1016/j.rinp.2019.102176.

[17] J. Ma, J. Wang, Z.-D. Hu, Z. Zhang, L. Pan, and A. Di Falco, "High-efficiency and ultrabroadband flexible absorbers based on transversely symmetrical multi-layer structures," *AIP Adv.*, vol. 9, no. 11, Nov. 2019, Art. no. 115007, doi: 10.1063/1.5119406.

[18] P. Upender, A. Kumar, and A. Kumar, "Design of a multiband graphene-based absorber for terahertz applications using different geometric shapes," *J. Opt. Soc. Amer. B, Opt. Phys.*, vol. 39, no. 1, pp. 188–199, Jan. 2022, doi: 10.1364/JOSAB.440757.

[19] G. Varshney and P. Giri, "Bipolar charge trapping for absorption enhancement in a graphene-based ultrathin dual-band terahertz biosensor," *Nanosc. Adv.*, vol. 3, no. 20, pp. 5813–5822, Oct. 2021, doi: 10.1039/d1na00388g.

[20] M. S. Khan, G. Varshney, and P. Giri, "Altering the multimodal resonance in ultrathin silicon ring for tunable THz biosensing," *IEEE Trans. Nanobiosci.*, vol. 20, no. 4, pp. 488–496, Oct. 2021, doi: 10.1109/TNB.2021.3105561.

[21] P. Upender and A. Kumar, "Ultrathin, ultra narrow band DMMA for biosensing applications," *IEEE Trans. Nanobiosci.*, vol. 22, no. 3, pp. 529–537, Jul. 2023, doi: 10.1109/TNB.2022.3217077.

[22] P. Upender and A. Kumar, "THz dielectric metamaterial sensor with high Q for biosensing applications," *IEEE Sensors J.*, vol. 23, no. 6, pp. 5737–5744, Mar. 2023, doi: 10.1109/JSEN.2023.3239669.

[23] X. Huang, W. Ye, J. Ran, Z. Zhou, R. Li, and B. Gao, "Highly sensitive biosensor based on metamaterial absorber with an all-metal structure," *IEEE Sensors J.*, vol. 23, no. 4, pp. 3573–3580, Feb. 2023, doi: 10.1109/JSEN.2023.3235897.

[24] Y. K. Srivastava, R. T. Ako, M. Gupta, M. Bhaskaran, S. Sriram, and R. Singh, "Terahertz sensing of 7 nm dielectric film with bound states in the continuum metasurfaces," *Appl. Phys. Lett.*, vol. 115, no. 15, Oct. 2019, Art. no. 151105, doi: 10.1063/1.5110383.

[25] R. Yahiaoui, A. C. Strikwerda, and P. U. Jepsen, "Terahertz plasmonic structure with enhanced sensing capabilities," *IEEE Sensors J.*, vol. 16, no. 8, pp. 2484–2488, Apr. 2016, doi: 10.1109/JSEN.2016.2521708.

[26] S. K. Patel and J. Parmar, "Highly sensitive and tunable refractive index biosensor based on phase change material," *Phys. B, Condens. Matter*, vol. 622, Dec. 2021, Art. no. 413357, doi: 10.1016/j.physb.2021.413357.

[27] A. S. Saadeldin, M. F. O. Hameed, E. M. A. Elkaramany, and S. S. A. Obayya, "Highly sensitive terahertz metamaterial sensor," *IEEE Sensors J.*, vol. 19, no. 18, pp. 7993–7999, Sep. 2019, doi: 10.1109/JSEN.2019.2918214.

[28] L. Cong, S. Tan, R. Yahiaoui, F. Yan, W. Zhang, and R. Singh, "Experimental demonstration of ultrasensitive sensing with terahertz metamaterial absorbers: A comparison with the metasurfaces," *Appl. Phys. Lett.*, vol. 106, no. 3, Jan. 2015, Art. no. 031107, doi: 10.1063/1.4906109.

[29] S. Banerjee, P. Dutta, A. V. Jha, B. Appasani, and M. S. Khan, "A biomedical sensor for detection of cancer cells based on terahertz metamaterial absorber," *IEEE Sensors Lett.*, vol. 6, no. 6, pp. 1–4, Jun. 2022, doi: 10.1109/LSENS.2022.3178918.

[30] A. Keshavarz and Z. Vafapour, "Sensing avian influenza viruses using terahertz metamaterial reflector," *IEEE Sensors J.*, vol. 19, no. 13, pp. 5161–5166, Jul. 2019, doi: 10.1109/JSEN.2019.2903731.

[31] Z. Vafapour, A. Keshavarz, and H. Ghahraloud, "The potential of terahertz sensing for cancer diagnosis," *Heliyon*, vol. 6, no. 12, Dec. 2020, Art. no. e05623, doi: 10.1016/j.heliyon.2020.e05623.

[32] M. B. Hossain, M. R. I. Faruque, A. S. Alshammari, and M. T. Islam, "Wide bandwidth enriched symmetric hexagonal split ring resonator based triple band negative permittivity metamaterial for satellite and Wi-Fi applications," *Results Phys.*, vol. 37, Jun. 2022, Art. no. 105511, doi: 10.1016/j.rinp.2022.105511.

[33] G. Wang, T. Wu, J. Jiang, Y. Jia, Y. Gao, and Y. Gao, "Switchable terahertz absorber from single broadband to triple-narrowband," *Diamond Rel. Mater.*, vol. 130, Dec. 2022, Art. no. 109460, doi: 10.1016/j.diamond.2022.109460.

[34] F. H. L. Koppens, D. E. Chang, and F. J. G. de Abajo, "Graphene plasmonics: A platform for strong light–matter interactions," *Nano Lett.*, vol. 11, no. 8, pp. 3370–3377, Aug. 2011, doi: 10.1021/nl201771h.

[35] F. H. L. MinovKoppensich, D. E. Chang, S. Thongrattanasiri, and F. J. G. G. de Abajo, "Graphene plasmonics: A platform for strong light-matter interactions," *Opt. Photon. News*, vol. 22, no. 12, p. 36, Dec. 2011, doi: 10.1364/opn.22.12.000036.

[36] P. Y. Liu, L. K. Chin, W. Ser, H. F. Chen, C.-M. Hsieh, C.-H. Lee, K.-B. Sung, T. C. Ayi, P. H. Yap, B. Liedberg, K. Wang, T. Bourouina, and Y. Leprince-Wang, "Cell refractive index for cell biology and disease diagnosis: Past, present and future," *Lab Chip*, vol. 16, no. 4, pp. 634–644, Feb. 2016, doi: 10.1039/c5lc01445j.

[37] M. Nejat and N. Nozhat, "Ultrasensitive THz refractive index sensor based on a controllable perfect MTM absorber," *IEEE Sensors J.*, vol. 19, no. 22, pp. 10490–10497, Nov. 2019, doi: 10.1109/JSEN.2019.2931057.

[38] O. Parkash, R. H. Shueb, and A. Ploss, "Diagnosis of dengue infection using conventional and biosensor based techniques," *Viruses*, vol. 7, no. 10, pp. 5410–5427, 2015, doi: 10.3390/v7102877.

[39] N. A. S. Omar, Y. W. Fen, J. Abdullah, Y. M. Kamil, W. M. E. M. Daniyal, A. R. Sadrolhosseini, and M. A. Mahdi, "Sensitive detection of dengue virus type 2 E-proteins signals using self-assembled monolayers/reduced graphene oxide-PAMAM dendrimer thin film-SPR optical sensor," *Sci. Rep.*, vol. 10, no. 1, p. 2374, Feb. 2020, doi: 10.1038/s41598-020-59388-3.

[40] J. A. Stewart, T. C. Holland, and A. S. Bhagwat, "Human herpes simplex virus-1 depletes APOBEC3A from nuclei," *Virology*, vol. 537, pp. 104–109, Nov. 2019, doi: 10.1016/j.virol.2019.08.012.

[41] V. A. Tang, A. K. Fritzsche, T. M. Renner, D. Burger, J. A. Lannigan, G. C. Brittain, C. V. Ouellet, E. van der Pol, and M. A. Langlois, "Engineered retroviruses as fluorescent biological reference particles for small particle flow cytometry," *BioRxiv*, Jun. 2019, Art. no. 614461, doi: 10.1101/614461.

[42] N. Ayyanar, G. T. Raja, M. Sharma, and D. S. Kumar, "Photonic crystal fiber-based refractive index sensor for early detection of cancer," *IEEE Sensors J.*, vol. 18, no. 17, pp. 7093–7099, Sep. 2018, doi: 10.1109/JSEN.2018.2854375.

[43] S. Banerjee, U. Nath, P. Dutta, A. V. Jha, B. Appasani, and N. Bizon, "A theoretical terahertz metamaterial absorber structure with a high quality factor using two circular ring resonators for biomedical sensing," *Inventions*, vol. 6, no. 4, p. 78, Nov. 2021, doi: 10.3390/inventions6040078.

[44] J. Zhang, N. Mu, L. Liu, J. Xie, H. Feng, J. Yao, T. Chen, and W. Zhu, "Highly sensitive detection of malignant glioma cells using metamaterial-inspired THz biosensor based on electromagnetically induced transparency," *Biosensors Bioelectron.*, vol. 185, Aug. 2021, Art. no. 113241, doi: 10.1016/j.bios.2021.113241.

PATRI UPENDER received the B.Tech. degree from JNTU Hyderabad, in 2008, the M.Tech. degree in RF and microwave from the Indian Institute of Technology Roorkee, in 2010, and the Ph.D. degree from the National Institute of Technology, Warangal, in 2023. He is currently an Assistant Professor with the School of Electronics Engineering, Vellore Institute of Technology, Chennai, Tamil Nadu, India. He has about ten years of research experience in the development of antennas and metamaterials. He has more than 30 publications in various journals and conferences at national and international level. His research interests include biosensing applications, metamaterials, dielectric resonator antennas, microwave, millimeter wave antennas, radar engineering, 5G devices, RF communication, and graphene devices.

S. PRASANNA BHARATHI received the B.Tech. degree in electronics and communication engineering from the SSN College of Engineering, University of Madras, the master's degree in microelectronics from Victoria University, Melbourne, Australia, and the Ph.D. degree in remote sensing from the Saveetha School of Engineering, SIMATS. He is currently an Assistant Professor with the Vellore Institute of Technology, Chennai. He has around 14 years of teaching experience and four years of industry experience. He has published around 25 papers in various reputed international journals and national and international conferences. His research interests include remote sensing, VLSI design, and the IoT. He is an Active Member of The Institution of Engineering and Technology (IET). He is the Vice Chairperson of the IET Chennai Local Network and Treasurer, The IET Communities Committee of South Asia.

SUKRITI received the B.Tech. degree from the Biju Patnaik University of Technology, India, in 2012, and the M.Tech. and Ph.D. degrees from the Indian Institute of Technology (Indian School of Mines) Dhanbad, India, in 2016 and 2022, respectively. She is currently an Assistant Professor with the School of Electronics Engineering, Vellore Institute of Technology, Chennai, India. She has authored six publications in international refereed journals and conference proceedings. Her research interests include signal processing and artificial intelligence in healthcare, biomedical, and wireless communication applications.

KRISHNA KUMBA received the B.Tech. degree in electrical and electronics engineering from JNTU Hyderabad, India, in 2008, the M.Tech. degree in the control system from the National Institute of Technology Kurukshetra, Haryana, India, in 2010, and the Ph.D. degree from the National Institute of Technology (NIT) Tiruchirappalli, Tiruchirappalli, India, in 2023. He is currently an Assistant Professor with the School of Electrical Engineering, Vellore Institute of Technology, Chennai, Tamil Nadu, India. His research interests include power system planning and reliability, solar photovoltaics, renewable energy systems, solar tracking systems, battery management systems, machine learning, and optimization.

AMARJIT KUMAR (Senior Member, IEEE) received the M.Tech. and Ph.D. degrees from the Indian Institute of Technology Roorkee, India, in 2012 and 2018, respectively. He is currently associated with the ECE Department, NIT Warangal, as an Assistant Professor. He has about ten years of research work experience in the development of passive and active RF circuits with concurrent multiband, reconfigurable, and multifunctional capabilities for next-generation wireless applications and development of RF/microwave sensors for the wireless monitoring of pressure and temperature variations for the industrial Internet of Things applications. He has designed, fabricated, and characterized reflection type microwave phase shifter, dual band tunable bandpass filters, Wilkinson power dividers, branch-line couplers, planar antennas, reconfigurable filtering dual band low-noise amplifiers, voltage-controlled oscillator, and wireless sensors using RF transceivers. He has published more than 40 research papers, one Indian patent, and three book chapters in reputed international journals and conferences. Some of the research works are published in IEEE TRANSACTIONS ON INSTRUMENTATION AND MEASUREMENT, IEEE SENSORS JOURNAL, IEEE TRANSACTIONS ON PLASMA SCIENCE, and IEEE TRANSACTIONS ON NANOBIOSCIENCE. His current research interests include design of millimeter-wave and Terahertz (THz) devices and biosensors for B5G and future 6G wireless communication systems. He served as a TPC member, the technical track chair, and the session chair for a number of IEEE conferences. He served as the Chairperson for the IEEE MTT Society SBC IIT Roorkee, from October 2013 to April 2018. He is serving as the Vice Chair for the IEEE Photonics Society Chapter of Hyderabad Section, India. He served as a reviewer for some of the reputed IEEE journals, letters, and transactions.

• • •